

Supporting Information

**Dynamic Features of Transition States for  $\beta$ -Scission Reactions of Alkenes over Acid Zeolites Revealed by AIMD Simulations**

*Jérôme Rey, Charles Bignaud, Pascal Raybaud, Tomáš Bučko,\* and Céline Chizallet\**

anie\_202006065\_sm\_miscellaneous\_information.pdf

**Abstract:** Zeolite-catalyzed alkene cracking is key to optimize the size of hydrocarbons. The nature and stability of intermediates and transition states (TS) are, however, still debated. We combine transition path sampling and blue moon ensemble density functional theory simulations to unravel the behavior of C<sub>7</sub> alkenes in CHA zeolite. Free energy profiles are determined, linking  $\pi$ -complexes, alkoxides and carbenium ions, for B<sub>1</sub> (secondary to tertiary) and B<sub>2</sub> (tertiary to secondary)  $\beta$ -scissions. B<sub>1</sub> is found to be easier than B<sub>2</sub>. The TS for B<sub>1</sub> occurs at the breaking of the C<C->C bond, while for B<sub>2</sub> it is the proton transfer from propenium to the zeolite. We highlight the dynamic behaviors of the various intermediates along both pathways, which reduce activation energies with respect to those previously evaluated by static approaches. We finally revisit the ranking of isomerization and cracking rate constants, which are crucial for future kinetic studies.

**DOI:** 10.1002/anie.2016XXXXX

**Table of Contents**

Table of Contents .....	2
Computational Procedures .....	3
S1. Supercell of chabazite .....	3
S2. Density functional theory calculations .....	3
S3. Transition Path Sampling simulations .....	4
S4. Blue Moon Sampling simulations .....	4
Results and Discussion .....	5
S5. Reactivity of the 4,4-dimethyl-penten-2-ium (I) in gas phase .....	5
S6. Characterization of reactant state (R) in chabazite .....	7
S7. Free energy profile for the isomerization step from R to I .....	8
S8. Type B <sub>1</sub> $\beta$ -scission from alkoxide or $\pi$ -complex .....	9
S8.1. Reaction starting from a $\pi$ -complex .....	10
S8.2. Reaction starting from an alkoxide .....	11
S9. Isomerization reaction from tertiary cation to $\pi$ -complex .....	12
S10. Kinetic modeling for the B <sub>1</sub> $\beta$ -scission mechanism .....	13
S11. Structural and charge analysis of the B <sub>1</sub> $\beta$ -scission transition structures .....	13
S12. Type B <sub>2</sub> $\beta$ -scission of 2-4-dimethyl-penten-2-ium .....	16
S12.1. Slow growth simulation .....	16
S12.2. Blue Moon sampling .....	17
References .....	18
Author Contributions .....	18

## Computational Procedures

### S1. Supercell of chabazite

CHA is a small window zeolite (maximal diameter of sphere that can diffuse along: 3.72 Å according to IZA<sup>[1]</sup>), but the cages are large (maximal diameter of sphere that can be included: 7.37 Å). In practical applications of alkene cracking, large pore zeolites are used, such as faujasite (7.35/11.24 Å) or zeolite Beta (5.95/6.68 Å). Due to the symmetry, these three frameworks (CHA, FAU, BEA\*), the number of atoms per primitive cell, however, differs a lot (36, 144, 192 respectively). The computational methods that we use here are, however, to date very difficult to perform for big cells such as the one of FAU and BEA\*. We estimated that the ratio between the computational time for BEA\* versus CHA is as high as 8. Thus, we chose the chabazite cell to get reliable results within a research-compatible time-scale.

A primitive rhombohedral cell of purely siliceous chabazite (CHA framework, symmetry group  $R\bar{3}m$ ), with 12 symmetry equivalent tetrahedral sites, was obtained from International Zeolite Association (IZA) database.<sup>[1]</sup> The cell was reoptimized yielding the lattice constants  $a = 9.336$  Å and  $\alpha = 94.6^\circ$ , which are in good agreement with the reference values<sup>1</sup> ( $a = 9.304$  Å and  $\alpha = 94.6^\circ$ ). The relaxed structure was subsequently used to build a supercell defined by lattice vectors  $\mathbf{a}'_1$ ,  $\mathbf{a}'_2$ , and  $\mathbf{a}'_3$  related to the primitive cell vectors of rhombohedral lattice ( $\mathbf{a}_1, \mathbf{a}_2, \mathbf{a}_3$ ) via the following transformations:  $\mathbf{a}'_1 = \mathbf{a}_2 + \mathbf{a}_3$ ,  $\mathbf{a}'_2 = \mathbf{a}_1 + \mathbf{a}_3$ , and  $\mathbf{a}'_3 = \mathbf{a}_1 + \mathbf{a}_2$ . The shortest interatomic separation between the atoms in hydrocarbon and atoms in its periodically repeated images in the supercell was at least 5.5 Å. The supercell is shown in Figure S1, where O<sup>1</sup> and O<sup>4</sup> oxygen atoms (following the labeling introduced in ref. <sup>[2]</sup>) involved in the transformations considered in this study are highlighted.

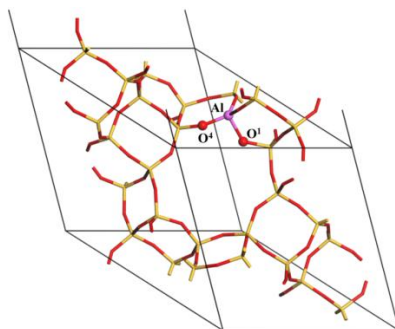


**Figure S1.** Unit cell of chabazite (Si in yellow, O in red, Al in purple). The proton is omitted in this representation as we started our investigations from a cation which has captured the proton of the acid site of the zeolite.

### S2. Density functional theory calculations

Periodic DFT calculations were performed using the VASP code.<sup>[3]</sup> The Kohn-Sham equations have been solved variationally in a plane-wave basis set using the projector augmented-wave (PAW) method of Blöchl,<sup>[4]</sup> as adapted by Kresse and Joubert.<sup>[5]</sup> The PBE exchange-correlation functional in the generalized gradient approximation proposed by Perdew et al.<sup>[6]</sup> was used. The D2 correction of Grimme<sup>[7]</sup> was applied to account for long-range dispersion interactions taking place upon the adsorption of hydrocarbon molecules in zeolites.<sup>[8]</sup> The Brillouin zone sampling was restricted to the  $\Gamma$ -point. A plane-wave cutoff energy of 400 eV was used in all calculations and the convergence criterion for the electronic self-consistency cycle was set to  $10^{-7}$  eV in geometry optimizations and  $10^{-6}$  eV in molecular dynamics simulations.

All relaxations related to the gas phase reactions were performed using the optimization engine GADGET<sup>[9]</sup> requiring that the forces acting on all atoms be smaller than 0.005 eV/Å. The cell used in these relaxations was the same as the supercell of chabazite (Section S1). The intrinsic reaction coordinate<sup>[10]</sup> (IRC) analysis has been employed using the damped velocity Verlet algorithm<sup>[11]</sup> in order to ensure that identified potential energy minima representing reactant and product states are linked by a common path on a potential energy landscape crossing a single first-order saddle point (transition state). The vibrational eigenspectra of resulting potential energy minima and saddle points have been examined in order to ensure that the number of imaginary frequencies was correct (i.e., zero for reactants and products and one for transition states).

Born Oppenheimer Molecular dynamics simulations (MD) have been performed in the NVT ensemble. All simulations were performed at the temperature  $T = 500$  K which is close to the relevant experimental conditions.<sup>[12]</sup> Its average value has been maintained by the Andersen thermostat<sup>[13]</sup> with a collision frequency per atom of  $0.01$  fs<sup>-1</sup>. The classical equations of motion were integrated using the leap-frog algorithm with an integration step of 1 fs. The atomic mass of tritium has been chosen for all H atoms in order to avoid numerical instabilities possibly caused by the use of a relatively large integration step.

The charge distribution of the atoms has been computed by iterative Hirshfeld charges<sup>[14]</sup> for different states (see Figure 3-c in the main text). The charge displayed is an average determined on 45 structures distributed evenly along the 45 ps long production period of the constrained MD run (after the 5 ps equilibration).

### S3. Transition Path Sampling simulations

Transition path sampling (TPS) is used to overcome the difficulties of the investigation of rare events in complex systems, for which the investigation of a few stationary points is insufficient to describe an energy landscape with uncountable saddle points.<sup>[15]</sup> In this method, an ensemble of reactive trajectories is harvested by a Monte Carlo procedure. The calculations have been performed by the same in-house code as in previous works.<sup>[16]</sup>

The initial reactive trajectory was obtained by joining two segments starting from a potential energy saddle point of the hydride shift between the secondary cations I and R (see later Figure S3) and generated by integrating equations of motion initiated with random generated (and Maxwell-Boltzmann distributed) atomic momenta forward and backward in time. In order to learn about the likely fate of I, a total of 200 shooting trial moves were performed,<sup>[15a]</sup> with an acceptance (being defined by the connection of reactant and a product) rate of 73 %. The length of trajectories was fixed to 500 fs, which was enough to describe the formation of the reactant (R) on the one side, and the intermediate secondary cation (I) or one of the products of its collapse on the other side. The approximation to reaction coordinate defined later in Equation S9, see later section S7) was used as an order parameter to distinguish reactant state ( $\xi < 1.2$ ) and product states ( $\xi > 1.7$ ), in whatever forms (secondary cation,  $\pi$ -complexes or alkoxides). The reactive trajectories harvested in the TPS simulations were subsequently integrated forward in time (up to a length of 2 ps) until the final stable products were formed. We emphasize that the purpose of this TPS investigation was to learn about the likely fate of the intermediate I rather than to quantify the individual transformation routes and hence we can report only qualitative statistics here.

The final states generated in the way described above were distributed as follows: 67.5 % ( $\pi$ -complexes), 13.0 % (alkoxides), 4.5 % (cracking products), 11.5 % (reactant R), 3 % (intermediate I). We checked that an equilibration done in the trajectory space has only a modest effect on our statistics: when initial 25% of trajectories were discarded, the percentages changed to 71.3 %, 9.3 %, and 4.7 % and when initial 50 % of trajectories were considered as equilibration, the percentages changed to 70.0 %, 11.0 %, and 3.0 %. We note that the presence of non-reactive routes (the ones that do not start in R and end in a product of a collapse of I different from R) is a consequence of the use of the abovementioned hybrid procedure in which the short trajectories generated in TPS were continued by a standard MD. When we exclude all such non-reactive trajectories, we arrive at the following distribution of products: 79.4 % ( $\pi$ -complexes), 15.3 % (alkoxides), 5.3 % (cracking products). Despite a qualitative character of these results, it is worth mentioning that they correctly reflect the relative stabilities determined accurately using the blue moon ensemble method (see Fig. 2 in the main text).

### S4. Blue Moon Sampling simulations

Free energies have been computed using the simulation protocol described in ref. <sup>[17]</sup>, which is based on the blue moon ensemble method,<sup>[18]</sup> as implemented in VASP.<sup>[19]</sup> The free-energy of activation ( $\Delta A^\ddagger$ ) for the process  $X \rightarrow Y$  is defined as follows:

$$\Delta A^\ddagger = \Delta A_{\xi_{ref,X} \rightarrow \xi^*} - k_B T \ln \left( \frac{h \langle |\dot{\xi}^*| \rangle}{k_B T} P(\xi_{ref,X}) \right), \quad \text{Eq. (S1)}$$

where  $\Delta A_{\xi_{ref,X} \rightarrow \xi^*}$  is a reversible work needed to shift the value of reaction coordinate ( $\xi$ ) from some arbitrary reference value characteristic for reactant ( $\xi_{ref,X}$ ) to the value  $\xi^*$  defining the free-energy transition state,  $\langle |\dot{\xi}^*| \rangle$  is the average velocity of reaction coordinate at the transition state, and  $P(\xi_{ref,X})$  is the probability density of the state  $\xi_{ref,X}$  in ensemble of all reactant (X) configurations. The term  $\Delta A_{\xi_{ref,X} \rightarrow \xi^*}$  is obtained from the bluemoon ensemble method,<sup>[18]</sup>  $P(\xi_{ref,X})$  can be determined using the straightforward MD simulations. The term  $\langle |\dot{\xi}^*| \rangle$  is determined using the constrained MD simulations via the formula<sup>[18a,20]</sup>

$$\langle |\dot{\xi}^*| \rangle = \sqrt{\frac{k_B T}{2\pi} \frac{1}{\langle Z^{-1/2} \rangle_{\xi^*}}}, \quad \text{Eq. (S2)}$$

where the term enclosed in  $\langle \dots \rangle_{\xi^*}$  is computed as a statistical average for a constrained ensemble with  $\xi(\mathbf{r}) = \xi^*$ , and  $Z$  the inverse mass metric tensor is:

$$Z = \sum_{i=1}^N \frac{1}{m_i} \sum_{\mu=x,y,z} \left( \frac{\partial \xi}{\partial r_{i,\mu}} \right)^2, \quad \text{(Eq. S3)}$$

with  $r_{i,\mu}$  being the Cartesian component  $\mu$  of position vector of an atom  $i$  and the sums are over all atoms and Cartesian components. We note that the term  $\langle Z^{-1/2} \rangle_{\xi^*}$  is readily available from the constrained MD performed for the state  $\xi^*$  within the  $\Delta A_{\xi_{ref,X} \rightarrow \xi^*}$  calculation.

Free energies of reaction ( $\Delta A_{X \rightarrow Y}$ ) are computed similarly:

$$\Delta A_{X \rightarrow Y} = \Delta A_{\xi_{ref,X} \rightarrow \xi_{ref,Y}} - k_B T \ln \left( \frac{P(\xi_{ref,X})}{P(\xi_{ref,Y})} \right). \quad \text{(Eq. S4)}$$

In Equation (2),  $\Delta A_{\xi_{ref,X} \rightarrow \xi_{ref,Y}}$  is the reversible work needed to shift the value  $\xi(\mathbf{r})$  from  $\xi_{ref,X}$  to some arbitrary reference value characteristic for product (Y),  $\xi_{ref,Y}$ , and  $P(\xi_{ref,Y})$  is the probability density of the state  $\xi_{ref,Y}$ .

By-reactions that can occur in our free energy calculations have been avoided by the use of restraining potentials. The addition of a restraining potential of the following form:

$$V(R) = \frac{1}{2}K(R - R_0)^2 \quad (\text{Eq. S5})$$

reinforced the 12 C-H bonds involving all hydrogen atoms except those which are involved in the reaction (on carbon atoms C<sup>3</sup> and C<sup>4</sup>, see Figure S3).  $R$  stands for the interatomic bonding distance C-H,  $R_0 = 1.1 \text{ \AA}$  is a constant corresponding approximately to the equilibrium length of the C-H bond, and the force constant  $K$  is set to  $100 \text{ eV.\AA}^{-2}$ .

The other possibilities of formation of  $\pi$ -complexes (formed upon deprotonation of C<sup>3</sup> and C<sup>4</sup> carbon atoms) and the formation of alkoxides between the C<sup>4</sup> atom of the secondary cation 4,4-dimethyl-penten-2-ium (I) and the two accessible oxygen atoms bonded to the aluminium atom of the zeolitic framework were prevented by the use of a smeared step potential. This potential (shown in Figure S2-a) acts on the distance  $R$  between the corresponding atoms. Its form is as follows:

$$V(R) = \frac{A_i}{1 + \exp\left(-D\left(\frac{R}{R_{0i}} - 1\right)\right)}, \quad (\text{Eq. S6})$$

where the parameters were set to the following values:  $A = -2 \text{ eV}$ ,  $D = 20$ ,  $R_{0,1} = 2.5 \text{ \AA}$  for the CO and  $R_{0,2} = 1.5 \text{ \AA}$  for the OH distance. It follows from the shape of this restraining potential that it generates extra forces acting on atoms only if a fluctuation occurs that attempts to create the C-O or O-H bonds involved.

The initial methyl shift requires a specific conformation of the reactant, denoted R(I) (see Figure S3-b). At 500 K, undesired rotations occur, causing discontinuities in the free energy gradients. Such uncontrolled rotations were prevented by using a smeared step potential acting on the dihedral angle ( $\tau$ ) between atoms C<sup>6</sup>-C<sup>2</sup>-C<sup>3</sup>-C<sup>7</sup>. This restraining potential is shown in Figure S2-b and its form was chosen as follows:

$$V(\tau) = \sum_{i=1}^2 \frac{A_i}{1 + \exp\left(-D_i\left(\frac{\tau}{\tau_{0,i}} - 1\right)\right)}, \quad (\text{Eq. S7})$$

where the parameters were set to the following values:  $A_1 = -2 \text{ eV}$ ,  $D_1 = 100$ ,  $\tau_{0,1} = 66 \text{ deg.}$ , and  $A_2 = 2 \text{ eV}$ ,  $D_2 = 20$ ,  $\tau_{0,2} = 129 \text{ deg.}$

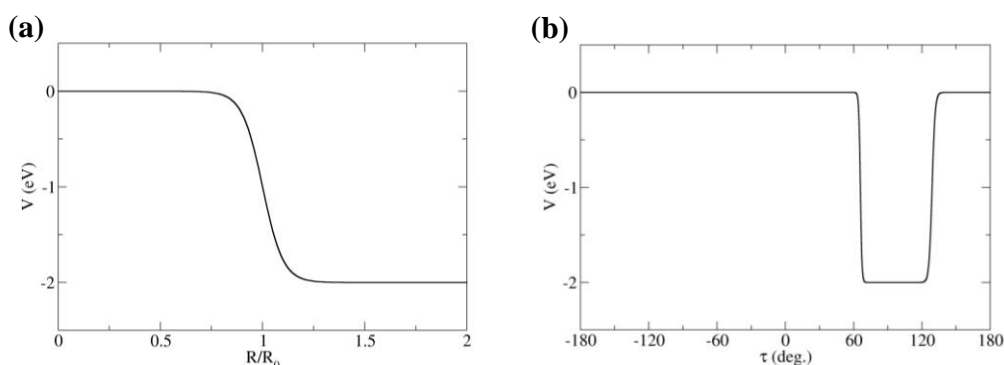


**Figure S2.** Restraining potentials acting on (a) a distance  $R$  between two atoms, (b) the dihedral angle C<sup>6</sup>-C<sup>2</sup>-C<sup>3</sup>-C<sup>7</sup> ( $\tau$ ).

## Results and Discussion

### S5. Reactivity of the 4,4-dimethyl-penten-2-ium (I) in gas phase

Free MD runs starting from I in gas phase or in chabazite revealed that many different spontaneous processes (including cracking) can occur. Among other reactions, isomerization into a more stable tertiary dibranched reactant, the 2,3-dimethyl-penten-2-ium tertiary cation R was observed. This is not surprising as all dibranched C<sub>7</sub> cations are expected to be connected one to another by fast type A isomerization reactions (including hydride and methyl shifts).<sup>[21]</sup>

Starting from a stable tertiary cation, the 2,3-dimethyl-penten-2-ium cation (R), the isomerization of R into the reactive secondary cation, the 4,4-dimethyl-penten-2-ium (I), proceeds via two type A isomerization steps (methyl and hydride shifts). The mechanism of isomerization (Figure S3) has been investigated by the static approach on the molecular system in gas phase.

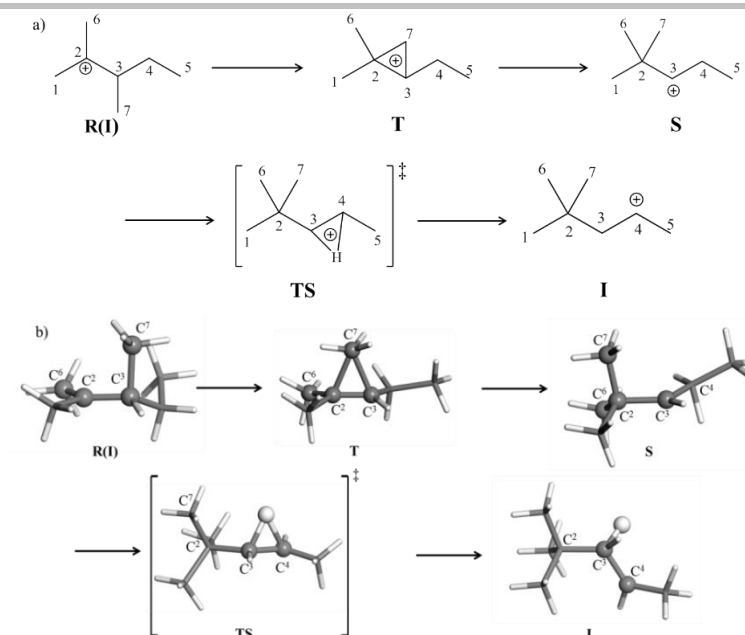


**Figure S3.** a) Mechanism of formation of the intermediate secondary cation I, starting from the rotational isomer R(I) of the reactant. Note that the corner protonated cyclopropane T and secondary cation S formed during the transformation between the reactant R(I) and the TS are not stationary points on the potential energy surface for the reaction in gas phase. The ball and sticks structures have been extracted from the constrained MD runs in chabazite.

The intrinsic reaction coordinate (IRC)<sup>[10]</sup> for the forward and backward reaction steps of the isomerization of the 2,3-dimethyl-penten-2-ium (R) into the reactive secondary cation, the 4,4-dimethyl-penten-2-ium (I), was identified using the damped velocity Verlet algorithm.<sup>[11]</sup> The result is shown in Figure S4-a. The transformation of the rotational isomer R(I) of the reactant begins with a methyl shift giving a highly unstable secondary cation (S) via a corner protonated cyclopropane (T) (Figure S3). S undergoes a subsequent hydride shift to give the secondary cation I. We emphasize that the structures T and S are not stationary points on the potential energy surface for the gas phase reaction (Figure S4). As already discussed in the literature, secondary cations such as S, with the positive charge on the carbon atom next to a quaternary carbon atom, are highly elusive species.<sup>[22]</sup> As a consequence, the unique transition state on the path connecting potential energy minima R(I) and I is located between the secondary cations S and I where a hydride shift takes place. IRC performed in the chabazite cell confirms these findings.

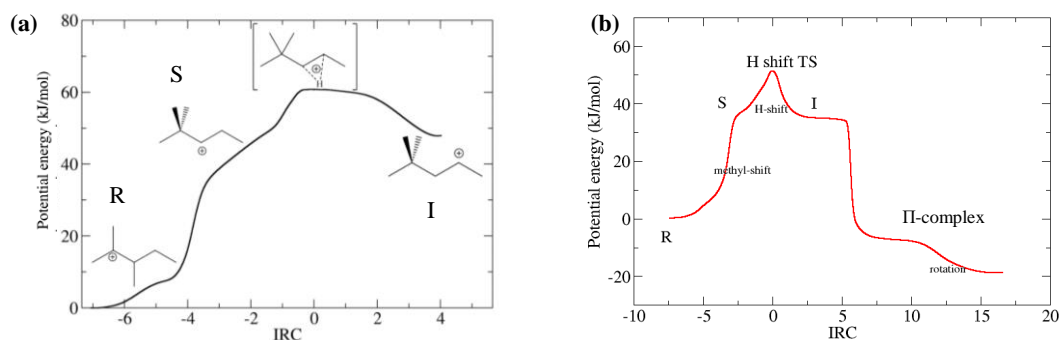


**Figure S4.** Potential energy profile along intrinsic reaction coordinate (IRC) for the isomerization reaction between 2,3-dimethyl-penten-2-ium cation (R) and 4,5-dimethyl-penten-2-ium cation (I) in gas phase (a), and in chabazite (b), the latter also includes the transformation of I into a  $\pi$ -complex.

Consistent with our previous work on isomerization reactions,<sup>[23]</sup> the IRC analysis for the gas phase reaction (Figure S4) showed that a specific rotational isomer R(I) is required for the initial methyl shift between the configurations R and S formed in the course of reaction. The dihedral angle ( $\tau$ ) defined by the sequence of atoms C<sup>6</sup>-C<sup>2</sup>-C<sup>3</sup>-C<sup>7</sup> (Figure S3) is the relevant parameter to control the geometry of the reactant. In the specific conformations involved in the C<sup>7</sup>H<sub>3</sub> methyl shift, the value of ( $\tau$ ) must be around  $\pm 90$  deg.

In order to determine if the cracking reaction of the secondary cation 4,4-dimethyl-penten-2-ium (I) is spontaneous, we realized a long (647 ps) free molecular dynamics run. We introduced bias potential to avoid that the two carbon atoms C<sup>2</sup> and C<sup>3</sup> involved in the broken bond move farther apart than 4 Å, which would prevent reformation of the C<sup>2</sup>-C<sup>3</sup> bond. A few tens of separatrix recrossings were observed. The free energy profile computed from probability distribution  $P(R)$ , with  $R$  the C<sup>2</sup>-C<sup>3</sup> distance, using  $\Delta A =$

$-k_B T \ln P(R)$  is shown in Figure S5. We can conclude that this cracking reaction in gas phase is an easy process, with a small free energy barrier.

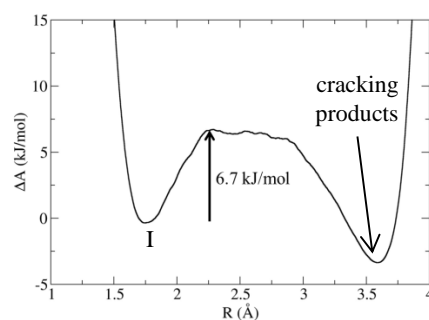


**Figure S5.** Free energy profile for the secondary cation 4,4-dimethyl-penten-2-ium (I) in gas phase as a function of the C<sup>2</sup>-C<sup>3</sup> distance (R), obtained with a long (647 ps) free molecular dynamics run.

### S6. Characterization of reactant state (R) in chabazite

The free energy of the reactant R in CHA as a function of  $\tau$  (defined by the sequence of atoms C<sup>6</sup>-C<sup>2</sup>-C<sup>3</sup>-C<sup>7</sup>) at T = 500 K has been determined by a blue moon simulation. The constrained simulations have been performed with 10 points evenly distributed in the range  $-90 \text{ deg.} \leq \tau < 90 \text{ deg.}$  The computed free energy profile is shown in Figure S6. Note that the periodicity  $A(\tau+180 \text{ deg.}) = A(\tau)$  follows from the symmetry of the reactant molecule. We identified two stable rotamers, hereafter labeled as R(I) and R(II) (Figure S7), corresponding to the minima on the free energy profile. The rotational isomer R(II) is 4.9 kJ/mol more stable than the state R(I) and the smallest barrier separating these two states is only 6.7 kJ/mol. The free energy profile  $A(\tau)$  has been used to compute the probability of occurrence of the rotamer R(I) defined by the formula:

$$p(R(I)) = \frac{\int_{\tau_{\max,1}}^{\tau_{\max,2}} \exp\left(-\frac{A(\tau)}{k_B T}\right) d\tau}{\int_{-180}^0 \exp\left(-\frac{A(\tau)}{k_B T}\right) d\tau}, \quad \text{Eq. (S8)}$$

where  $\tau_{\max,1}$  and  $\tau_{\max,2}$  are the maxima on the free energy profile separating R(I) and R(II). The computed value for  $p(R(I))$  is 20.9 %.

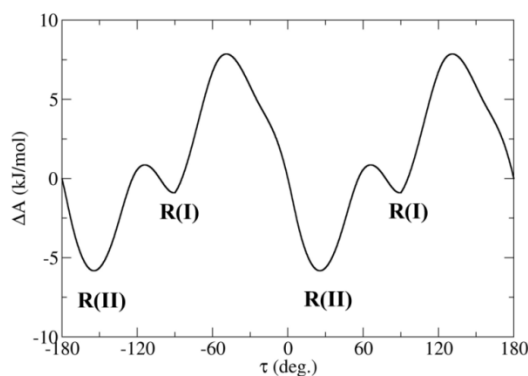


**Figure S6.** Free energy profile as a function of the torsion angle  $\tau$  defined by the carbon atoms C<sup>6</sup>, C<sup>2</sup>, C<sup>3</sup>, and C<sup>7</sup> in the reactant (R) adsorbed in chabazite. Note that periodic boundary conditions apply, i.e., the point  $\tau = -180 \text{ deg.}$  is identical to the point  $\tau = 180 \text{ deg.}$

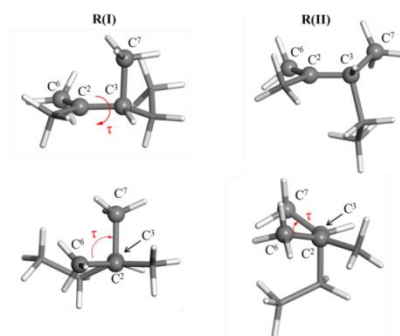


**Figure S7.** Rotational isomers R(I) ( $\tau \approx 90$  deg.) and R(II) ( $\tau \approx 30$  deg.) of the reactant 2,3-dimethyl-penten-2-ium cation. Top panels: side view; bottom panels: front view was chosen so that the atom C<sup>2</sup> overlaps the atom C<sup>3</sup>.

### S7. Free energy profile for the isomerization step from R to I

We used for this reaction the following approximation to reaction coordinate,  $\xi$  (Equation S9) which drives the methyl shift of C<sup>7</sup>H<sub>3</sub> from C<sup>3</sup> to C<sup>2</sup> and the hydride shift of one hydrogen atom of C<sup>4</sup> to C<sup>3</sup>.  $\xi$  is invariant with respect to the interchange of the three methyl groups C<sup>1</sup>H<sub>3</sub>, C<sup>6</sup>H<sub>3</sub>, C<sup>7</sup>H<sub>3</sub> and of the three hydrogen atoms H<sup>a</sup>, H<sup>b</sup> and H<sup>c</sup> of C<sup>3</sup> and C<sup>4</sup> (the numbering of atoms is given in Figure S3).

$$\xi = \sum_{j=1,6,7} \eta(C^2 - C^j) - \sum_{j=1,6,7} \eta(C^3 - C^j) + \sum_{j=a,b,c} \eta(C^3 - H^j) - \sum_{j=a,b,c} \eta(C^4 - H^j) \quad \text{Eq. (S9)}$$

where  $\eta(A - B)$  is the coordination number of the A-B bond:<sup>[24]</sup>

$$\eta(A - B) = \frac{1 - \left(\frac{d(A - B)}{d_{A-B,ref}}\right)^9}{1 - \left(\frac{d(A - B)}{d_{A-B,ref}}\right)^{14}}, \quad \text{Eq. (S10)}$$

with  $d_{C-C,ref} = 1.7 \text{ \AA}$  being the reference length for the C-C bonds and  $d_{C-H,ref} = 1.3 \text{ \AA}$  the reference length for the C-H bonds.

Upon integration of free energy gradients computed for a grid of 16 points, we obtained the free energy profile shown in Figure S8. The initial part of the profile, from the reference state R(I) ( $\xi_{ref,R} = 0.11$ ) to S ( $\xi \approx 0.9$ ), corresponds to the methyl shift. An hydride shift transforms S into the secondary cation 4,4-dimethyl-penten-2-ium (I). The transition state is located at  $\xi^* = 2.1$ . The value of the term  $\Delta A_{\xi_{ref,R} \rightarrow \xi^*}$  is  $60.3 \pm 3.8 \text{ kJ/mol}$ . The free energy of activation  $\Delta A^\ddagger$  is determined via Equation S1. The computed value of the velocity term ( $\langle |\dot{\xi}| \rangle$ ) is  $1.9 \cdot 10^{13} \text{ s}^{-1}$ . The term  $P(\xi_{ref,R})$  cannot be computed efficiently in a straightforward MD run because of the free energy barrier separating R(I) and R(II). Following the computational strategy suggested in our previous work,<sup>[23]</sup> we express  $P(\xi_{ref,R})$  as a product of two terms computed separately:

$$P(\xi_{ref,R}) = \tilde{P}(\xi_{ref,R}) p(R(I)), \quad \text{Eq. (S11)}$$

where  $\tilde{P}(\xi_{ref,R})$  is the probability density of the configuration  $\xi_{ref,R}$  among the configurations of rotational isomer R(I), and  $p(R(I))$  is the probability to find the rotamer R(I) among all reactant configurations.

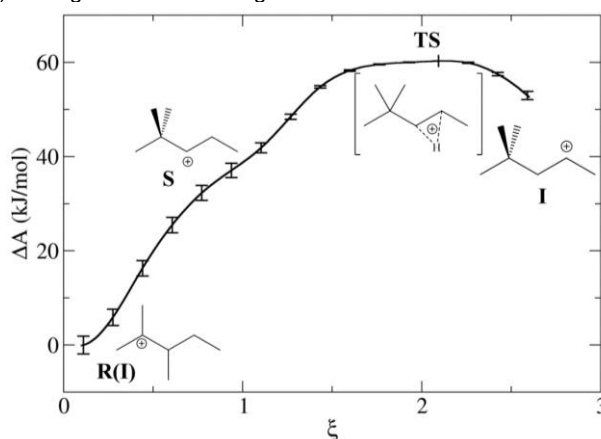


**Figure S8.** Free energy profile ( $\Delta A(\xi)$ ) computed at 500 K using the blue moon ensemble approach for the isomerization reaction from R to I in chabazite.

Figure S9 shows the probability distribution function  $\tilde{P}(\xi_{ref,R})$  for the rotational isomer R(I) of the reactant R. A restraining potential acting on the dihedral angle C<sup>6</sup>-C<sup>2</sup>-C<sup>3</sup>-C<sup>7</sup> ( $\tau$ ) has been used to prevent interconversions between rotational isomers R(I) and R(II) (see section S5). The length of production runs of MD simulations was 175 ps (the initial 5 ps were considered as equilibration and the corresponding data were discarded). The numerical value of  $\tilde{P}(\xi_{ref,R})$  for  $\xi_{ref,R} = 0.11$  is 4.58.

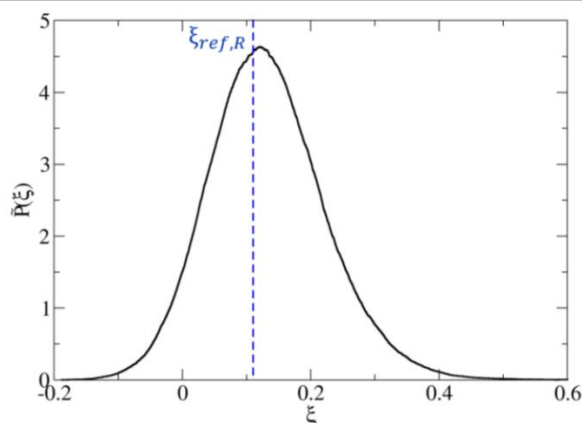


**Figure S9.** Probability distribution function  $\bar{P}(\xi)$  computed for the reactant state R(I).

The value of  $p(R(I))$  was obtained in blue moon simulations, and is 0.209 (see Section S6). The resulting free energy of activation  $\Delta A^\ddagger$  is  $60.9 \pm 3.8$  kJ/mol.

Thus, it appears that the two type A isomerizations needed to connect R with I are consecutive and not synchronous, and moreover, S (obtained after methyl shift) is not defined as an intermediate on the free energy surface, contrary to the general belief. The TS is the one that connects the two secondary carbenium ions S and I.

The probability distributions of the C–C and C–H bond involved in the transition state is given in Figure S10. This TS is in fact related to the 1,2 H-shift process. The C<sup>3</sup>–H<sup>a</sup> bond is much shorter than C<sup>4</sup>–H<sup>a</sup> bond, signifying that the structure of the transition state is closer to the secondary cation (I) than to the highly unstable secondary cation (S). The structure of the transition state optimized in the static approach in gas phase is even more dissymmetric, the C<sup>3</sup>–H<sup>a</sup> bond being much shorter and C<sup>4</sup>–H<sup>a</sup> much longer than in MD.

Such a difference between MD results in zeolite and static results in gas phase was already observed for secondary cations in our previous work:<sup>[23a]</sup> the structure of secondary cations is very constrained at 0 K and more flexible on the free energy surface at finite temperature. The calculation of the free energy of reaction is complicated by the fact that the secondary cation 4,4-dimethyl-penten-2-ium (I) formed after crossing the free energy barrier is not stable in a MD run that is long enough to collect a sufficient statistics, which is caused by the fact that this metastable cation can readily undergo many different transformations. As a consequence, only a qualitative estimate of the free energy of I is reported in Figure 2 in the main text.

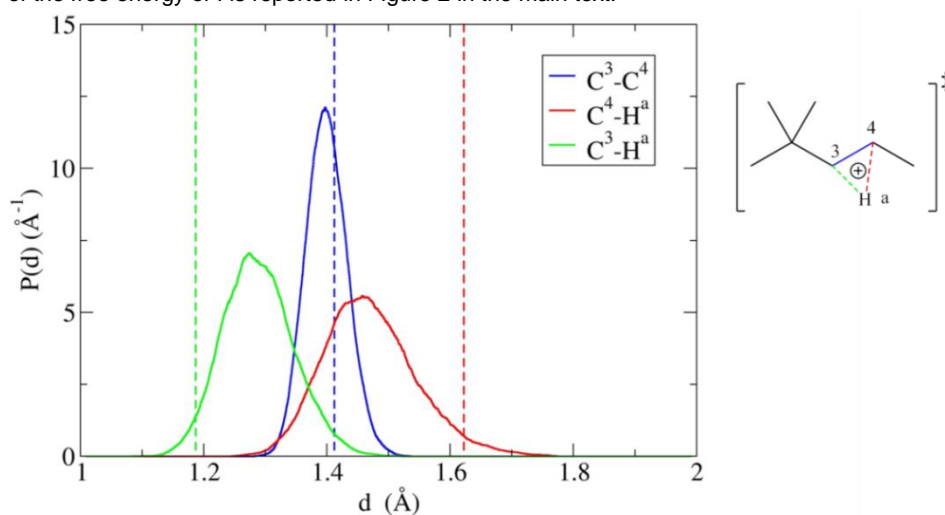


**Figure S10.** Probability distributions of C–C and C–H bonds involved in the transition state of 1,2 H-shift determined using MD at 500 K. The static approach results for the gas phase reaction are indicated by vertical dashed lines.

### S8. Type B<sub>1</sub> β-scission from alkoxide or π-complex

Thanks to TPS (see main text), we demonstrated that the transformation of the secondary cation 4,4-dimethyl-penten-2-ium (I) into alkoxide or π-complex is more likely than the direct cracking. In this section, the free energetics of type B<sub>1</sub> β-scission starting from alkoxide and π-complex is thus investigated. The mechanisms and the numbering of atoms are described in Figure S11. The

reactants (4,4-dimethyl-pent-2-oxide and (E)-4,4-dimethyl-pent-2-ene adsorbed on the oxygen atom O<sup>4</sup>) were considered in our analysis as they were formed as predominant products in our TPS simulations.

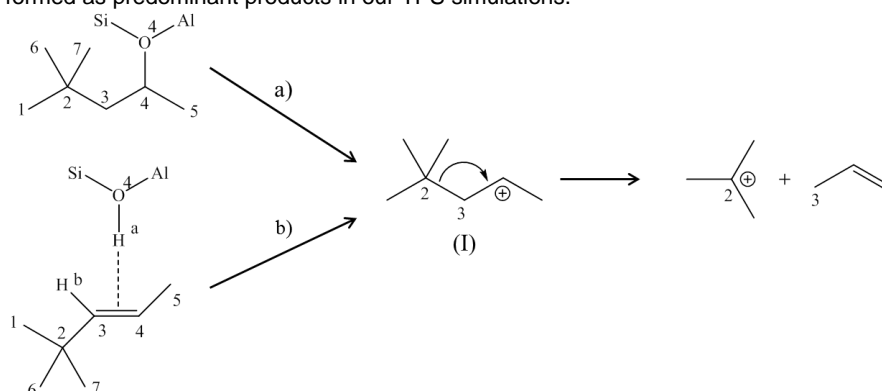


**Figure S11.** Mechanisms of the type B<sub>1</sub>  $\beta$ -scission starting from an alkoxide (a) or a  $\pi$ -complex (b), with the numbering of atoms used in the definition of the approximation to reaction coordinate.

### S8.1. Reaction starting from a $\pi$ -complex

For this reaction, the following approximation to reaction coordinate was used to drive the protonation of the  $\pi$ -complex and the breaking of the C<sup>2</sup>-C<sup>3</sup> bond:

$$\xi = \eta(C^3 - H^a) + \eta(C^3 - H^b) - \eta(C^2 - C^3), \quad \text{Eq. (S12)}$$

where the coordination number  $\eta(A - B)$  is defined in Equation S10, with  $d_{C-H,ref} = 1.3 \text{ \AA}$  and  $d_{C-C,ref} = 1.7 \text{ \AA}$ .

By-reactions were avoided by addition of a restraining potential reinforcing the 12 C-H bonds not involved in the reaction coordinate ( $\xi$ ) as described in Section S4. The formation of alkoxides was prevented for the points near the secondary cation ( $\xi \approx 1$ ) by the use of a smeared step potential as described in Section S4. Figure S12 shows the probability distribution functions  $P(\xi_{ref,R})$  and  $P(\xi_{ref,P})$  for the reactant R and product P of the reaction. The length of the run of MD simulations was 150 ps for the reactant and 130 ps for the product (the first 5 ps were considered as equilibration and the corresponding data were discarded). For the reactant, the numerical value of  $P(\xi_{ref,R})$  for  $\xi_{ref,R} = 0.16$  is 3.27 and for the product,  $P(\xi_{ref,P}) = 4.19$  for  $\xi_{ref,P} = 1.70$ .

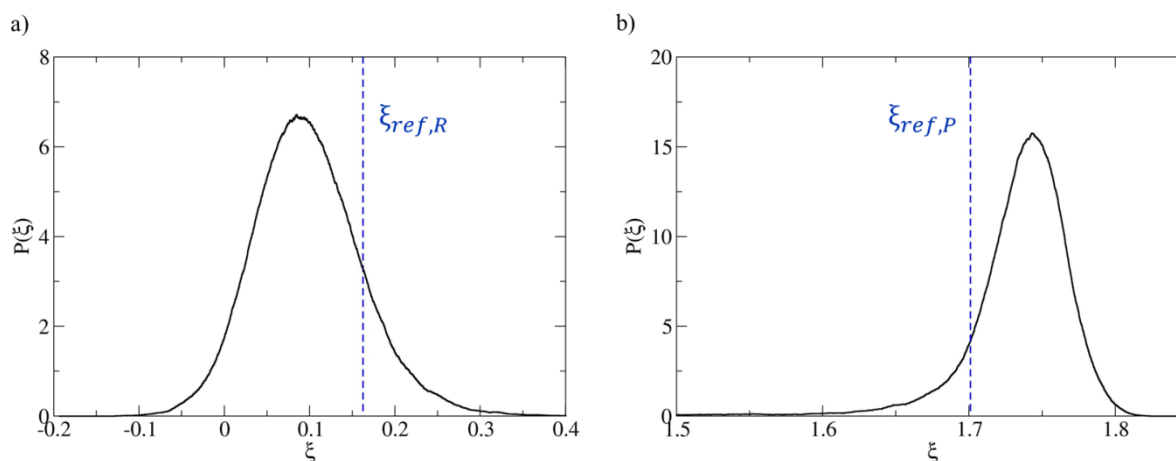


**Figure S12.** Probability distribution functions  $P(\xi)$  for the reactant (a) and product (b) for the cracking mechanism B<sub>1</sub> starting from a  $\pi$ -complex.

The blue moon simulations have been performed using 20 integration points along  $\xi$  and the resulting free energy profile is displayed in Figure S13.a. In the first part of the profile, from  $\xi_{ref,R} = 0.16$  to  $\xi = 0.95$ , the proton transfer between the zeolite and the chemisorbed alkene takes place, giving the secondary cation (I) which appears as a very shallow local minimum. Then, from  $\xi \approx 0.95$  to  $\xi_{ref,P} = 1.70$ , the cracking occurs: the C<sup>2</sup>-C<sup>3</sup> bond is broken and tert-butylum cation and propene are formed. The transition state for cracking is located at  $\xi^* \approx 1.45$ .

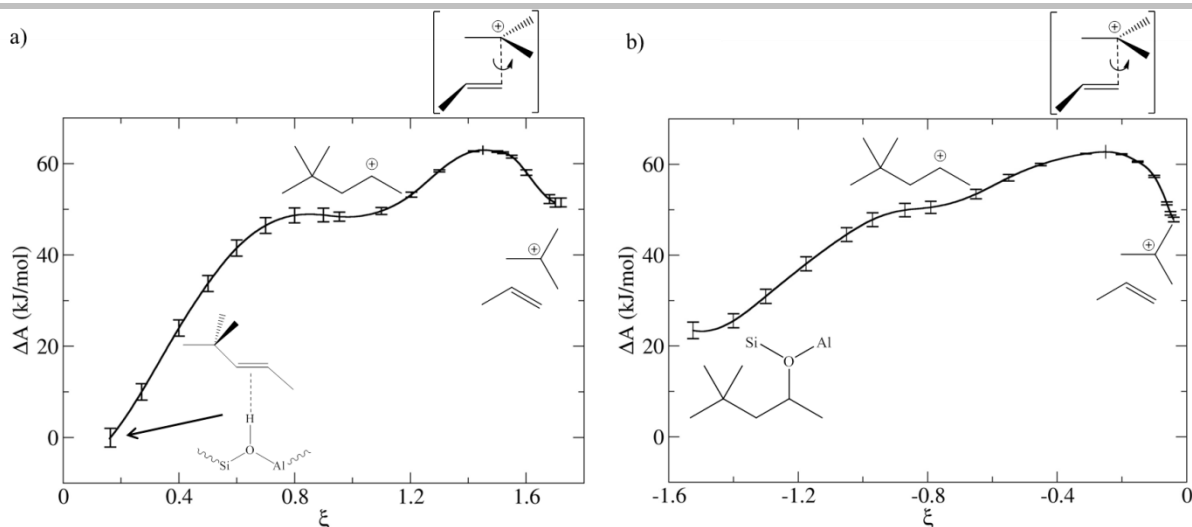


**Figure S12.** Free energy profiles ( $A(\xi)$ ) computed using the blue moon ensemble approach for a) the type  $B_1$   $\beta$ -scission starting from a  $\pi$ -complex, and b) the type  $B_1$   $\beta$ -scission starting from an alkoxide, in chabazite at  $T = 500$  K. The profile b) has been shifted to set the free energy of the transition state to the same level as that of the profile a)..

The values of the terms  $\Delta A_{\xi_{ref,R} \rightarrow \xi^*}$ ,  $P(\xi_{ref,R})$  and  $\langle |\dot{\xi}^*| \rangle$  needed to determine  $\Delta A^\ddagger$  are  $63.0 \pm 4.2$  kJ/mol, 3.27 and  $1.27 \cdot 10^{13} \text{ s}^{-1}$ , respectively. The resulting value of free energy of activation computed using Equation S1 is  $60.1 \pm 4.2$  kJ/mol. Finally, the free energy of reaction, computed using Equation S4 is  $52.5 \pm 4.6$  kJ/mol, whereby the terms  $\Delta A_{\xi_{ref,R} \rightarrow \xi_{ref,P}} = 51.5 \pm 4.6$  kJ/mol and  $P(\xi_{ref,P}) = 4.19$  have been employed.

### S8.2. Reaction starting from an alkoxide

For this reaction, the following approximation to reaction coordinate was used to describe the desorption of the alkoxide and the breaking of the  $C^2-C^3$  bond:

$$\xi = -\eta(O^4 - C^4) - \eta(C^2 - C^3), \quad \text{Eq. (S13)}$$

where  $\eta(A-B)$  is the coordination number of the A-B bond (Equation S10) with  $d_{ref} = 1.7 \text{ \AA}$  for C-C and C-O bonds. The numbering of atoms is defined in Figure S11.

By-reactions were avoided by addition of a restraining potential reinforcing the 15 C-H bonds as described in Section S4.

Figure S13 shows the probability distribution function  $P(\xi_{ref,R})$  and  $P(\xi_{ref,P})$  for the reactant R and product P of the reaction. The length of the run of MD simulations was 148 ps for the reactant and 128 ps for the product (the first 5 ps being considered as equilibration and discarded). For the reactant, the numerical value of  $P(\xi_{ref,R})$  for  $\xi_{ref,R} = -1.52$  is 4.44 and for the product,  $P(\xi_{ref,P}) = 7.13$  for  $\xi_{ref,P} = -0.040$ .

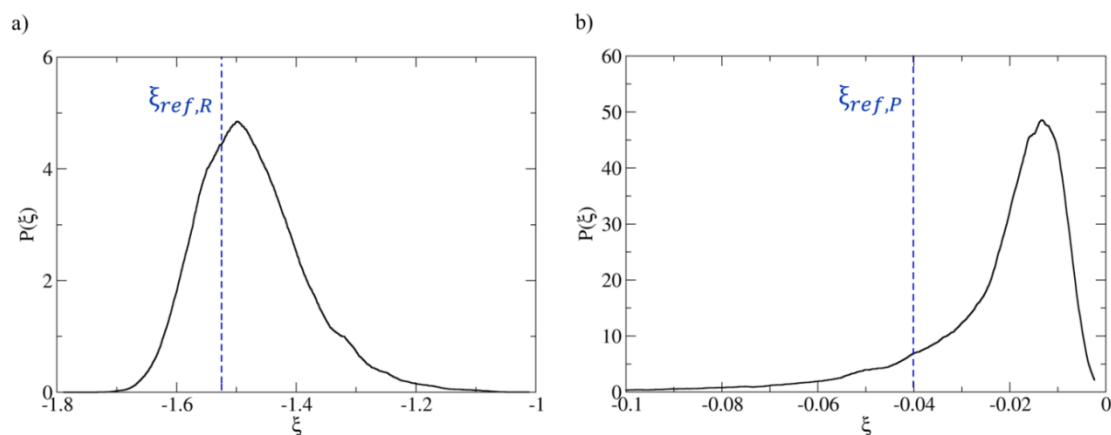


**Figure S13.** Probability distribution functions  $P(\xi_{ref})$  for the reactant (a) and product (b) of the cracking mechanism  $B_1$  starting from an alkoxide.

The blue moon simulations have been performed using 19 integration points along  $\xi$ . The computed free energy profile is displayed in Figure S12.b. In the first part of the profile, from  $\xi_{ref,R} = -1.52$  to  $\xi \approx -0.79$ , the O<sup>3</sup>-C<sup>4</sup> bond is broken and the secondary cation 4,4-dimethyl-penten-2-ium (I) is formed. It is localized in a flat zone of the free energy profile. In the next stage of reaction occurring in the interval between  $\xi \approx -0.79$  and  $\xi_{ref,P} = -0.04$ , the C<sup>2</sup>-C<sup>3</sup> bond is broken, forming tert-butyl cation and propene. The transition state is located at  $\xi^* \approx -0.25$ . The value of the term  $\Delta A_{\xi_{ref,R} \rightarrow \xi^*}$  is  $39.3 \pm 3.7$  kJ/mol.

The free energy of activation  $\Delta A^\ddagger$  is determined employing the terms  $\langle |\dot{\xi}^*| \rangle = 3.2 \cdot 10^{12} \text{ s}^{-1}$  and  $P(\xi_{ref,R}) = 4.44$ . The computed value of  $\Delta A^\ddagger$  is  $40.9 \pm 3.7$  kJ/mol. Finally, the free energy of reaction, computed using Equation (2) combined with the terms  $\Delta A_{\xi_{ref,R} \rightarrow \xi_{ref,P}} = 24.4 \pm 3.8$  kJ/mol and  $P(\xi_{ref,P}) = 7.13$  is  $26.4 \pm 3.8$  kJ/mol. Both activation and reaction energies are much lower than those reported previously by static approaches starting with alkoxides (reaction energy > 60 kJ/mol, up to 125 kJ/mol, see ref. [25]), showing that an accurate sampling as afforded by AIMD is required.

### S9. Isomerization reaction from tertiary cation to $\pi$ -complex

In this section we describe the blue moon simulation performed to connect the tertiary cation 2,3-dimethyl-penten-2-ium (R) to the  $\pi$ -complex (E)-4,4-dimethyl-pent-2-ene used as reactant for cracking reaction. The approximation to reaction coordinate must drive smoothly this transformation, with a methyl shift of C<sup>7</sup>H<sub>3</sub> from C<sup>4</sup> to C<sup>3</sup> and a proton transfer from C<sup>4</sup> to an oxygen atom O<sup>4</sup>. We used for this reaction the following approximation to reaction coordinate, which is invariant with respect to the interchange of the three methyl groups C<sup>1</sup>H<sub>3</sub>, C<sup>6</sup>H<sub>3</sub>, C<sup>7</sup>H<sub>3</sub> and of the three hydrogen atoms of C<sup>3</sup> and C<sup>4</sup> (the numbering of atoms is as in Figure S3):

$$\xi = \sum_{j=1,6,7} \eta(C^2 - C^j) - \sum_{j=1,6,7} \eta(C^3 - C^j) - \sum_{j=a,b} \eta(C^4 - H^j) + \sum_{j=a,b} \eta(O^4 - H^j), \quad \text{Eq. (S14)}$$

where  $\eta$  is the coordination number (Equation S10) and  $a$  and  $b$  are the two hydrogen atoms initially located on C<sup>4</sup>.

As described in Section S4, 12 harmonic springs were used to reinforce the C-H bonds of all carbon atoms except C<sup>3</sup> and C<sup>4</sup> which were involved in the reaction coordinate. The dihedral angle ( $\tau$ ) between atoms C<sup>6</sup>-C<sup>2</sup>-C<sup>3</sup>-C<sup>7</sup> was restrained on the first points of the simulation to ensure that the required rotamer of the reactant was involved in the methyl shift.

The free energy profile obtained with 16 integration points is shown in Figure S14. In the first part of the profile, from  $\xi_{ref,R} = -0.82$  to  $\xi \approx 0.1$ , the methyl shift from C<sup>4</sup> to C<sup>3</sup> occurs. The resulting highly unstable secondary cation transfers a proton between the C<sup>4</sup> atom and the O<sup>4</sup> atom of the zeolite. The transition state ( $\xi^* \approx 0.33$ ) corresponds to this proton transfer. The value of the term  $\Delta A_{\xi_{ref,R} \rightarrow \xi^*}$  is  $47.1 \pm 3.2$  kJ/mol and  $\Delta A_{\xi_{ref,R} \rightarrow \xi_{ref,P}} = 1.7$  kJ/mol. The free energy of activation  $\Delta A^\ddagger$  is determined via Equation S1. The value of the term  $\langle |\dot{\xi}^*| \rangle$  computed as described in Section S4 is  $1.82 \cdot 10^{13} \text{ s}^{-1}$ .

Figure S15 shows the probability distribution function  $P(\xi_{ref,R})$  and  $P(\xi_{ref,P})$  for the reactant R (2,3-dimethyl-penten-2-ium cation) and product P ((E)-4,4-dimethyl-pent-2-ene) of the reaction. The lengths of the MD runs were 194 ps and 186 ps for the reactant and product, respectively (in both cases, the initial 5 ps were considered as equilibration and the corresponding data were discarded). For the reactant, the numerical value of  $\tilde{P}(\xi_{ref,R})$  for  $\xi_{ref,R} = -0.82$  is 4.43 and for the product,  $P(\xi_{ref,P}) = 3.26$  for  $\xi_{ref,P} = 1.72$ . The term  $P(\xi_{ref,R})$  is computed using the same value  $p(R(I)) = 20.9\%$  (see Section S6). Finally, the computed free energy of activation  $\Delta A^\ddagger$  is  $48.0 \pm 3.4$  kJ/mol and the free energy of reaction is  $7.0 \pm 3.4$  kJ/mol.

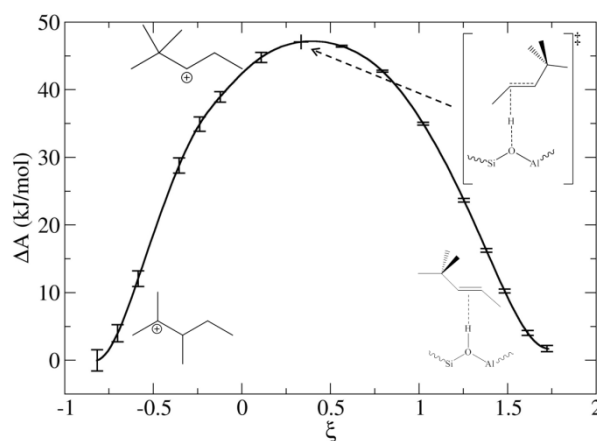


**Figure S14.** Free energy profile computed using the blue moon ensemble approach for the transformation of the tertiary cation (2,3-dimethyl-penten-2-ium) to the  $\pi$ -complex ((E)-4,4-dimethyl-pent-2-ene).

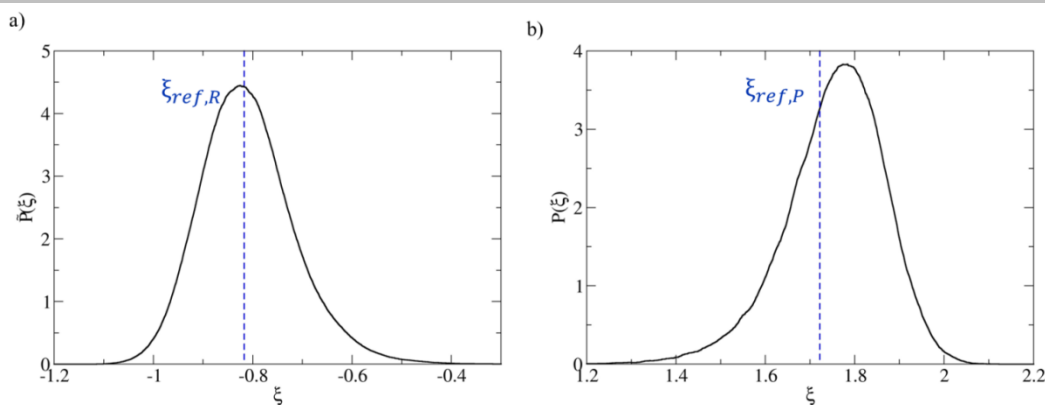


**Figure S15.** Probability distribution functions  $P(\xi_{ref})$  for the reactant (a) and product (b) for the transformation of the tertiary cation to the  $\pi$ -complex (B1 cracking).

### S10. Kinetic modeling for the B<sub>1</sub> $\beta$ -scission mechanism

In order to compare relative importance of the two competing reaction mechanisms  $R \rightarrow I$  and  $R \rightarrow \pi$  of transformation of reactant state R into cracking products P, a simple kinetic model has been built, shown in Figure S16-a.

The rate equations have been solved using a simple Euler method with a time steps of  $10^{-13}$  s. The following initial concentrations have been considered:

- Simulation A:  $c_R(0) = 1 \text{ mol/m}^3$ , all other initial concentrations being at  $0 \text{ mol/m}^3$ .
- Simulation B:  $c_{PI}(0) = 1 \text{ mol/m}^3$ , all other initial concentrations being at  $0 \text{ mol/m}^3$ .

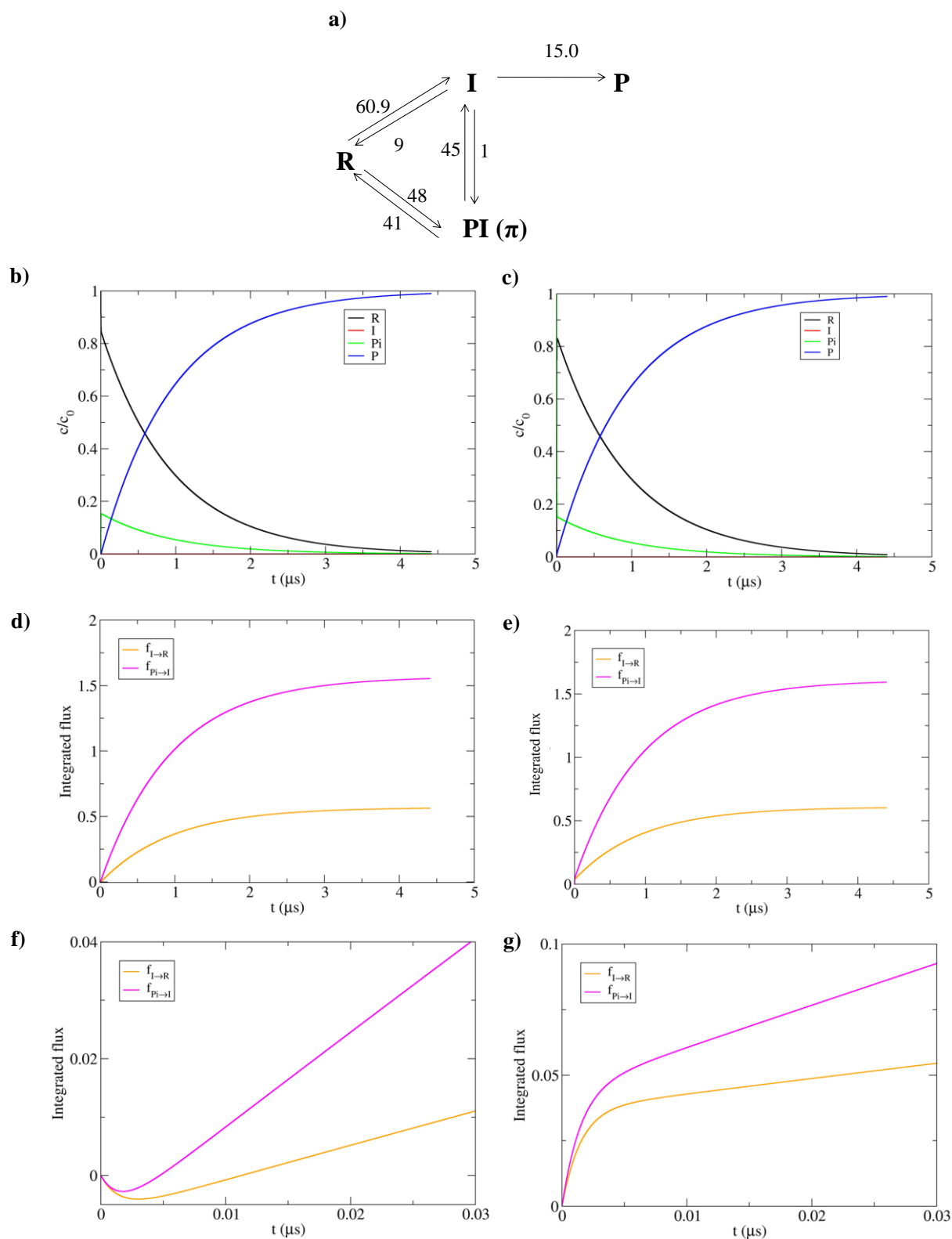


**Figure S16.** (a) Kinetic scheme used for the comparison of the two competing reaction mechanisms  $R \rightarrow I$  and  $R \rightarrow \pi$  of transformation of reactant state  $R$  into cracking products  $P$ . The free energy barriers (kJ/mol) for each forward and backward steps are shown on the corresponding arrows and come from blue moon ensemble simulations. (b)-(c) Time evolution of concentration of individual states considered in the kinetic model, for simulations A ( $c_R(0) = 1 \text{ mol/m}^3$ ) and B ( $c_{PI}(0) = 1 \text{ mol/m}^3$ ), respectively, (d)-(g) integrated fluxes defined in the text, for simulation A (d)-(f), simulation B (e)-(g).

The rate constants have been computed from the Eyring equation<sup>[26]</sup> using the blue moon free energy barriers. The integration was stopped at 99% conversion in cracking products  $P$ .

In order to determine the relative importance of reactions  $R \rightarrow I$  and  $R \rightarrow \pi \rightarrow I$ , integrated fluxes to I were computed for both alternatives as follows:

$$f_{R \rightarrow I}(\tau) = \int_0^\tau dt \{k_{R \rightarrow I} c_R - k_{I \rightarrow R} c_I\}$$

and

$$f_{\pi \rightarrow I}(\tau) = \int_0^\tau dt \{k_{\pi \rightarrow I} c_\pi - k_{I \rightarrow \pi} c_I\}$$

where  $k_{X \rightarrow Y}$  is the rate constant for the transformation from X to Y and  $c_X$  is the concentration of the state X. Figures S16 a and b show the time evolution of concentration of states R, I,  $\pi$ , and P determined for the simulations A and B. The time evolution of fluxes  $f_{R \rightarrow I}$  and  $f_{\pi \rightarrow I}$  shown in Figures S16 c and d indicate that I is formed mainly via the reaction  $\pi \rightarrow I$ , which is consistent with the lower barrier of the  $R \rightarrow \pi$ -complex with respect to the  $R \rightarrow I$  transformation. Besides a short induction period evident in Figures S16 e and f, the time evolutions observed in simulations A and B are nearly identical.

### S11. Structural and charge analysis of the B1 $\beta$ -scission transition structures

The probability distributions of the C–C and C–H bond involved in the transition state of the isomerization of the stable tertiary cation (the 2,3-dimethyl-penten-2-ium cation R) into the reactive secondary cation (the 4,5-dimethyl-penten-2-ium I) are shown in Figure S17. As evident from Figure S18 showing the electron localization function (ELF),<sup>[27]</sup> the C<sub>3</sub> and C<sub>4</sub> fragments of this TS are not covalently bonded.

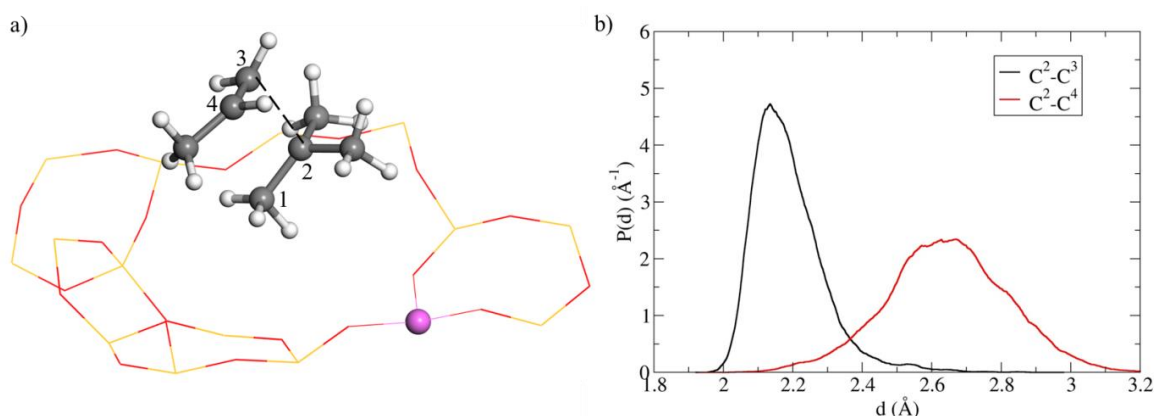


**Figure S17.** a) A selected structure from the constrained MD simulation of the transition state of the type B<sub>1</sub> cracking reaction starting from the  $\pi$ -complex (E)-4,4-dimethyl-pent-2-ene. The average C<sup>2</sup>–C<sup>3</sup> distance is around 2.2 Å, and the average C<sup>2</sup>–C<sup>4</sup> distance is around 2.6 Å. b) Probability distributions of the C<sup>2</sup>–C<sup>3</sup> and C<sup>2</sup>–C<sup>4</sup> distances involved in the transition state of the type B<sub>1</sub> cracking reaction starting from the  $\pi$ -complex (E)-4,4-dimethyl-pent-2-ene determined using MD at 500 K.

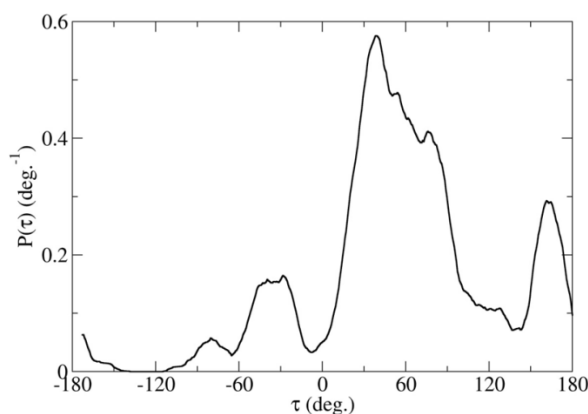


**Figure S18.** Probability distributions of dihedral angle ( $\tau$ ) defined by the sequence of atoms C<sup>1</sup>–C<sup>2</sup>–C<sup>3</sup>–C<sup>4</sup> involved in the transition state of the type B<sub>1</sub> cracking reaction starting from the  $\pi$ -complex (E)-4,4-dimethyl-pent-2-ene determined using MD at 500 K.

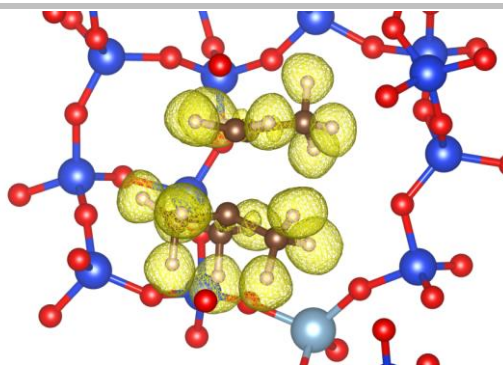


**Figure S19.** Electron localization function isosurface (ELF=0.9) for a selected transition structure from the constrained MD simulation of the transition state of the type B<sub>1</sub> cracking reaction starting from the  $\pi$ -complex (E)-4,4-dimethyl-pent-2-ene. Note that absence of ELF basins between C<sub>3</sub> and C<sub>4</sub> moieties indicates that these fragments are not covalently bonded.

## S12. Type B<sub>2</sub> $\beta$ -scission of 2-4-dimethyl-penten-2-ium

Figure S20 presents the reaction under consideration and the atom numbering.

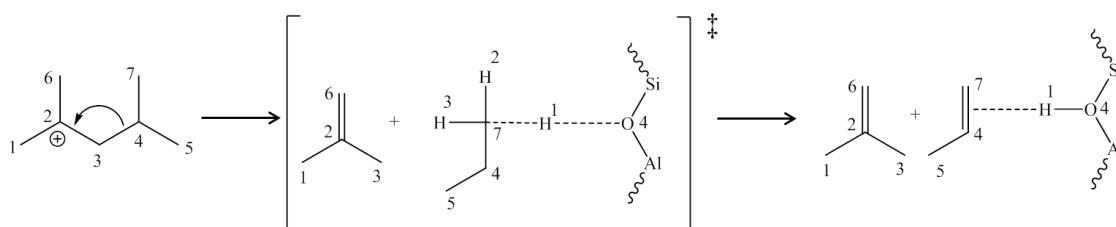


**Figure S20.** Mechanism of type B<sub>2</sub> cracking of 2-4-dimethyl-penten-2-ium in adsorbed propene and isobutene.

### S12.1. Slow growth simulation

We employed qualitatively a slow growth simulation protocol<sup>[28]</sup> (MD in which a CV is increased at a constant rate) to check if the candidate CV (defined in Eq. S15 below) can drive smoothly the reaction from the reactant to the product state. The results are shown in Figure S21. Despite a rather high transformation rate ( $5.3 \cdot 10^{-2} \text{ ps}^{-1}$ ), only a modest hysteresis was observed for two different directions of transformation, which is a good indication of reversibility of the process driven by the given CV. We note that no discontinuity occurs owing to the inclusion of the proton transfer between the propenium cation and the zeolite.<sup>[29]</sup>

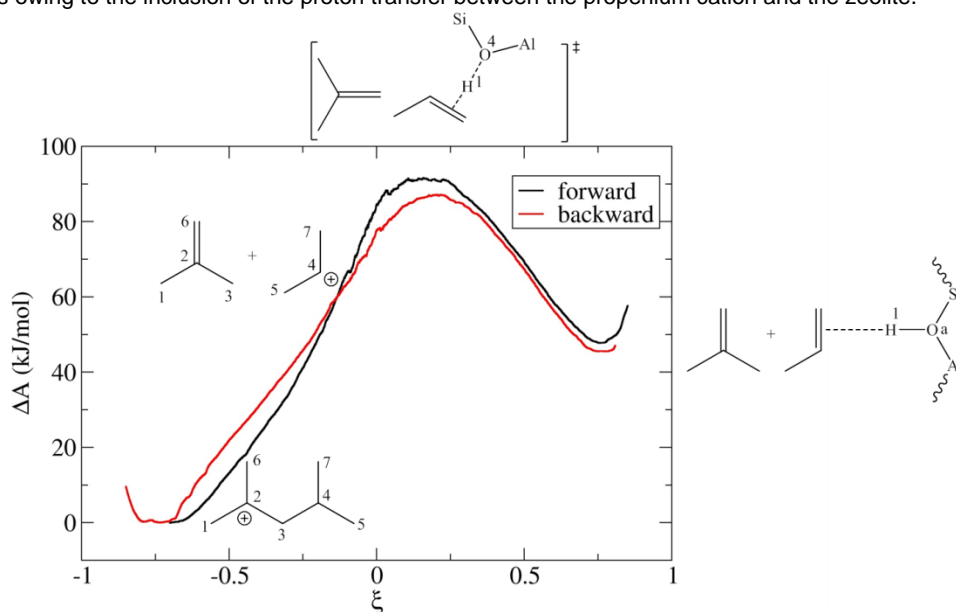


**Figure S21.** Forward and backward slow growth simulations for the type B<sub>2</sub>  $\beta$ -scission of 2-4-dimethyl-penten-2-ium in isobutene and  $\pi$  complex of propene. The approximation to reaction coordinate is defined in Equation S15 in section S12.2.

## S12.2. Blue Moon sampling

We used for this reaction the following approximation to the reaction coordinate, which involves the C<sup>3</sup>-C<sup>4</sup> bond broken in the transformation and the O-H bond in formation:

$$\xi = -\eta(C^3 - C^4) + \sum_{\substack{i=5,7 \\ j=1,2,3}} \eta(O^4 - H_{C^i}^j), \quad \text{Eq. (S15)}$$

where  $\eta(A - B)$  is the coordination number of the  $A - B$  bond,  $H_{C^i}^j$  is the hydrogen atom  $j$  on the carbon atoms  $i$  of the propenium fragment, and  $O^4$  is the relevant oxygen atom of the zeolitic framework.

No undesired by-reaction was observed and the blue moon simulation was performed without any restraints.

The results are shown in Figure 4-a of the main text. The value of the term  $\Delta A_{\xi_{ref,R} \rightarrow \xi^*}$  is  $86.8 \pm 5.3$  kJ/mol.

Figure S22 shows the probability distribution function  $P(\xi_{ref,R})$  and  $P(\xi_{ref,P})$  for the reactant R and products P of the reaction. The length of the run of MD simulations was 150 ps for the reactant and 200 ps for the products (out of which the first 5 ps were considered as equilibration and discarded). For the reactant, the numerical value of  $P(\xi_{ref,R})$  for  $\xi_{ref,R} = -0.70$  is 5.79 and for the product,  $P(\xi_{ref,P}) = 6.57$  for  $\xi_{ref,P} = 0.75$ .

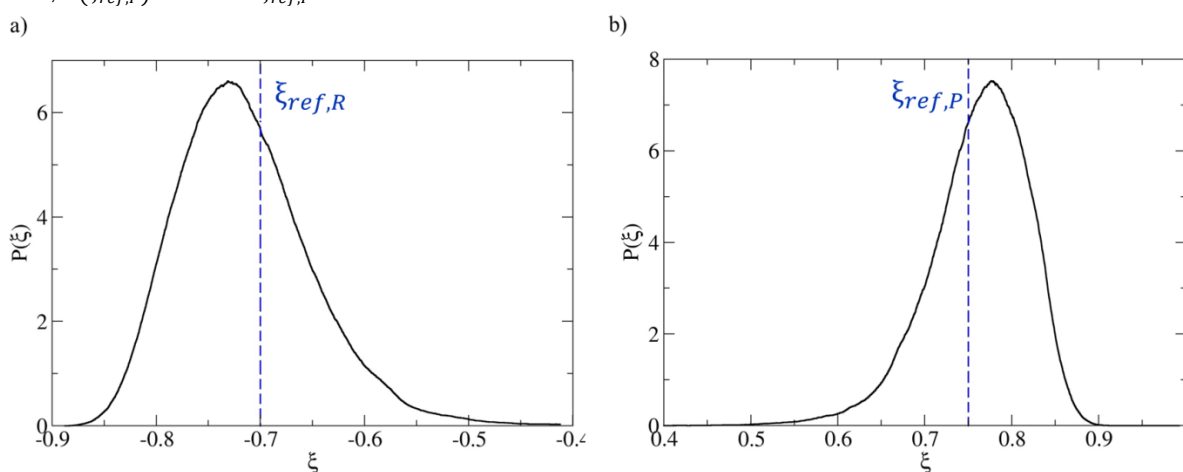


**Figure S22.** Probability distribution functions  $P(\xi)$  for the reactant (a) and product (b) of the B<sub>2</sub>  $\beta$ -scission of 2-4-dimethyl-penten-2-ium reaction.

The free energy of activation  $\Delta A^\ddagger = 84.4 \pm 5.3$  kJ/mol is determined via Equation S1, using  $\langle |\dot{\xi}^*| \rangle = 6.5 \cdot 10^{12} \text{ s}^{-1}$ , and  $P(\xi_{ref,R}) = 5.79$ . Employing Equation S4 together with the probability density for the product state ( $P(\xi_{ref,R}) = 6.57$ ), a free energy of reaction of  $46.3 \pm 5.4$  kJ/mol was obtained.

## References

- [1] C. Baerlocher, J. K. McCusker, *Database of Zeolite Structures*: <http://www.iza-structure.org/databases/>.
- [2] L. J. Smith, A. Davidson, A. K. Cheetham, *Catal. Lett.* **1997**, *49*, 143-146.
- [3] a) G. Kresse, J. Hafner, *Phys. Rev. B* **1993**, *47*, 558-561; b) G. Kresse, J. Hafner, *Phys. Rev. B* **1994**, *49*, 14251-14269; c) G. Kresse, J. Furthmüller, *Comput. Mat. Sci.* **1996**, *6*, 15-50.
- [4] P. E. Blöchl, *Phys. Rev. B* **1994**, *50*, 17953-17979.
- [5] G. Kresse, D. Joubert, *Phys. Rev. B* **1999**, *59*, 1758-1775.
- [6] J. Perdew, K. Burke, M. Ernzerhof, *Phys. Rev. Lett.* **1996**, *77*, 3865-3868.
- [7] a) S. Grimme, *J. Comput. Chem.* **2006**, *27*, 1787-1799; b) T. Bucko, J. Hafner, S. Lebegue, J. G. Angyan, *J. Phys. Chem. A* **2010**, *114*, 11814-11824.
- [8] F. Göttl, A. Grüneis, T. Bucko, J. Hafner, *J. Chem. Phys.* **2012**, *137*, 114111.
- [9] a) T. Bučko, J. Hafner, J. G. Angyán, *J. Chem. Phys.* **2005**, *122*, 124508; b) T. Bučko, *Theoretical Chemistry Accounts* **2018**, *137*, 164.
- [10] a) K. Fukui, *J. Phys. Chem.* **1970**, *74*, 4161-4163; b) K. Fukui, *Acc. Chem. Res.* **1981**, *14*, 363-368.
- [11] H. P. Hratchian, H. B. Schlegel, *J. Phys. Chem. A* **2002**, *106*, 165-169.
- [12] a) A. Patriceon, E. Benazzi, C. Travers, J. Y. Bernhard, *Catal. Today* **2001**, *65*, 149-155; b) G. G. Martens, G. B. Marin, J. A. Martens, P. A. Jacobs, G. V. Baron, *J. Catal.* **2000**, *195*, 253-267.
- [13] D. Frenkel, B. Smit, *Understanding Molecular Simulation*, Academic Press, **2002**.
- [14] a) P. Bultinck, C. van Alsenoy, P. W. Ayers, R. Carbó-Dorca, *J. Chem. Phys.* **2007**, *126*, 144111; b) T. Bučko, S. Lebegue, J. Hafner, J. G. Angyán, *J. Chem. Theory Comput.* **2013**, *9*, 4293-4299.
- [15] a) C. Dellago, P. G. Bolhuis, P. L. Geissler, in *Adv. Chem. Phys.*, John Wiley & Sons, Inc., **2003**, pp. 1-78; b) P. G. Bolhuis, D. Chandler, C. Dellago, P. L. Geissler, *Annu. Rev. Phys. Chem.* **2002**, *53*, 291-318.
- [16] a) T. Bucko, L. Benco, O. Dubay, C. Dellago, J. Hafner, *J. Chem. Phys.* **2009**, *131*, 214508; b) T. Bučko, L. Benco, J. Hafner, J. G. Angyán, *J. Catal.* **2011**, *279*, 220-228; c) T. Bučko, J. Hafner, *J. Catal.* **2015**, *329*, 32-48.
- [17] T. Bučko, S. Chibani, J.-F. Paul, L. Cantrel, M. Badawi, *Phys. Chem. Chem. Phys.* **2017**, *19*, 27530-27543.
- [18] a) E. A. Carter, G. Ciccotti, J. T. Hynes, R. Kapral, *Chem. Phys. Lett.* **1989**, *156*, 472-477; b) G. Ciccotti, M. Sprick, *J. Chem. Phys.* **1998**, *109*, 7737-7744.
- [19] T. Bucko, *J. Phys. Condens. Matter.* **2008**, *20*, 064211.
- [20] N. E. Henriksen, F. Y. Hansen, *Theories of Molecular Reaction Dynamics: The Microscopic Foundation of Chemical Kinetics*, Oxford University Press, **2008**.
- [21] a) C. Marcilly, *Acido-Basic Catalysis*, Technip, Paris, **2005**; b) J. Weitkamp, *ChemCatChem* **2012**, *4*, 292-306; c) P. Raybaud, A. Patriceon, H. Toulhoat, *J. Catal.* **2001**, *197*, 98-112.
- [22] P. Cnudde, K. De Wispelaere, L. Vanduyfhuys, R. Demuyne, J. Van der Mynsbrugge, M. Waroquier, V. Van Speybroeck, *ACS Catal.* **2018**, *8*, 9579-9595.
- [23] a) J. Rey, P. Raybaud, C. Chizallet, T. Bučko, *ACS Catal.* **2019**, *9*, 9813-9828; b) J. Rey, A. Gomez, P. Raybaud, C. Chizallet, T. Bučko, *J. Catal.* **2019**, *373*, 361-373.
- [24] M. Iannuzzi, A. Laio, M. Parrinello, *Phys. Rev. Lett.* **2003**, *90*, 238302.
- [25] a) A. M. Rigby, G. J. Kramer, R. A. van Santen, *J. Catal.* **1997**, *170*, 1-10; b) J. P. Hay, A. Redondo, Y. Guo, *Catal. Today* **1999**, *50*, 517-523; c) S. Namuangruk, P. Pantu, J. Limtrakul, *ChemPhysChem* **2005**, *6*, 1333-1339; d) Y.-X. Sun, J. Yang, L.-F. Zhao, J.-X. Dai, H. Sun, *J. Phys. Chem. C* **2010**, *114*, 5975-5984; e) Y. Chu, B. Han, A. Zheng, F. Deng, *J. Phys. Chem. C* **2012**, *116*, 12687-12695; f) M. N. Mazar, S. H. Al Hashimi, M. Cococcioni, A. Bhan, *J. Phys. Chem. C* **2013**, 23609-23620; g) Y.-H. Guo, M. Pu, B.-H. Chen, F. Cao, *Appl. Catal. A* **2013**, *455*, 65-70; h) B. Huang, P. Bai, M. Neurock, R. J. Davis, *Appl. Catal. A* **2017**, *546*, 149-158.
- [26] H. Eyring, *J. Chem. Phys.* **1935**, *3*, 107-115.
- [27] B. Silvi, A. Savin, *Nature* **1994**, *371*, 683-686.
- [28] T. K. Woo, P. M. B. P. E. Magl, T. Ziegler, *J. Phys. Chem. B* **1997**, *101*, 7877-7880.
- [29] P. Cnudde, K. De Wispelaere, J. Van der Mynsbrugge, M. Waroquier, V. Van Speybroeck, *J. Catal.* **2017**, *345*, 53-69.

## Author Contributions

JR and CB performed the calculations. TB, CC and PR designed the research program and supervised the whole study. CC and PR obtained the funding from the scientific Division of IFPEN. The original draft of the paper was written by JR, with further contributions of all authors.